International Journal of Heat and Mass Transfer 217 (2023) 124623

Contents lists available at ScienceDirect

International Journal of Heat and Mass Transfer

journal homepage: www.elsevier.com/locate/ijhmt

Impact of external turbulence on film cooling designs using large eddy simulations

Lukas Fischer *, Michael Pfitzner

University of the Bundeswehr Munich, Department of Aerospace Engineering, Institute of Thermodynamics, Werner-Heisenberg-Weg 39, Neubiberg, 85577, Bavaria, Germany

ARTICLE INFO

Keywords:
Film cooling
Heat transfer
Unsteady high turbulence boundary conditions
Computational fluid dynamics (CFD)
Large eddy simulation (LES)

ABSTRACT

Large Eddy Simulations (LES) of film cooling flows were conducted to investigate the impact of high turbulence intensity in the main flow, representative of jet-engine combustor conditions. A comparison was made with LES simulations at zero turbulence at the main flow inlet boundary. The study investigated three different film cooling configurations, which involved cylindrical holes and two variations with holes embedded in trenches known as transverse and segmented trench. Different momentum ratios ($I = 3.5$ and 8.3) relevant to combustor flows in jet-engines were applied. The LES simulations utilized OpenFOAM and solved the energy and passive scalar transport equations to determine film cooling efficiency (η), heat transfer coefficient (h_f), and net heat flux reduction ($NHFR$). The numerical results were validated through comparison with experimental data. The mean and instantaneous results revealed that high turbulence intensity in the main flow significantly influenced film cooling performance. The film cooling efficiency was found to decrease with increased turbulence intensity, while for the ordinary film cooling design exhibiting jet lift-off, the increased mixing led to higher η. The heat transfer coefficient increased with turbulence intensity and momentum ratio, with turbulence intensity having a greater impact on ordinary designs and momentum ratio on trenched designs. Moreover, increasing turbulence intensity or momentum ratio resulted in lower $NHFR$ for all designs. Hot spots were observed in the instantaneous results, with spatial variations depending on the film cooling design.

1. Introduction

The efficiency of jet engines is significantly affected by the turbine inlet temperature. The hot gas temperature in the combustion chamber and turbine often exceeds the maximum limit of the material temperature. To prevent damaging to the metal walls of these parts, film cooling techniques are used. These techniques typically involve the use of cylindrical and fan-shaped holes to create a layer of coolant film [1,2]. However, with a trench, which might be formed during the application of thermal barrier coating (TBC), the effectiveness of the cooling can be improved [3,4]. Both designs are shown in Fig. 1.

Film cooling holes embedded into trenches reduce jet lift-off from the wall and provide improved lateral spreading of the coolant.

Researchers have used Reynolds-Averaged Navier-Stokes (RANS) simulations to study adiabatic film cooling effectiveness (η) at the wall:

$$\eta = \frac{T_\infty - T_{aw}}{T_\infty - T_c} \tag{1}$$

where T_∞ and T_c represent the temperatures of the hot gas and coolant, respectively, while T_{aw} denotes the adiabatic wall temperature. It has been found that a steady-state RANS approach is not often sufficient for accurately predicting the mean flow field and film cooling efficiency [5]. Although many optimization processes rely on the steady-state assumption [6,7], recent studies have shown that unsteady RANS simulations can significantly improve the prediction of film cooling effectiveness. Sperling's research [8] found that incorporating the dominant frequency from the broadband spectrum of the velocity signal at the inlet upstream of the film cooling injection in unsteady RANS simulations leads to more accurate results. This highlights the importance of considering the unsteadiness of the inlet boundary conditions when predicting film cooling effectiveness. Additionally, studies using Large Eddy Simulation (LES) have demonstrated good agreement with experimental data under low turbulence conditions [9–11].

The turbulent hot gas flow field affects the jets that originate from effusion cooling holes located in the combustor or turbine. The turbu-

* Corresponding author.
E-mail address: L.Fischer@unibw.de (L. Fischer).

https://doi.org/10.1016/j.ijheatmasstransfer.2023.124623
Received 10 June 2023; Received in revised form 6 July 2023; Accepted 18 August 2023
Available online 30 August 2023

Nomenclature

Roman Symbols

D	Film cooling hole diameter
c	Specific heat
f	Frequency
h	Heat transfer coefficient or enthalpy
I	Momentum ratio
Pr	Prandtl number
$\dot{q}$	Heat flux
Re	Reynolds number
t	Time
T	Temperature or period length of a signal
Tu	Turbulence intensity
u, v, w	Velocity components
x, y, z	Cartesian coordinates

Greek Symbols

η	Adiabatic film cooling efficiency
θ	Non-dimensionalized temperature
Λ	Turbulence length scale
ρ	Density
δ	Boundary layer thickness

Subscripts

a	Adiabatic
aw	Adiabatic wall
c	Cold gas
d	Distance boundary layer growth
f	With film cooling
i	Index
p	Constant pressure
s	Sensible
w	Wall
0	Without film cooling
99	99% Freestream velocity
∞	Hot gas freestream

Superscripts

$\bar{\bullet}$	Averaged
$\bullet'$	Fluctuation
$\tilde{\bullet}$	Filtered

Abbreviations

CFD	Computational Fluid Dynamics
LES	Large Eddy Simulation
NHFR	Net Heat Flux Reduction
RANS	Reynolds-Averaged Navier-Stokes
RMS	Root Mean Square
TPIV	Thermographic Particle Image Velocimetry

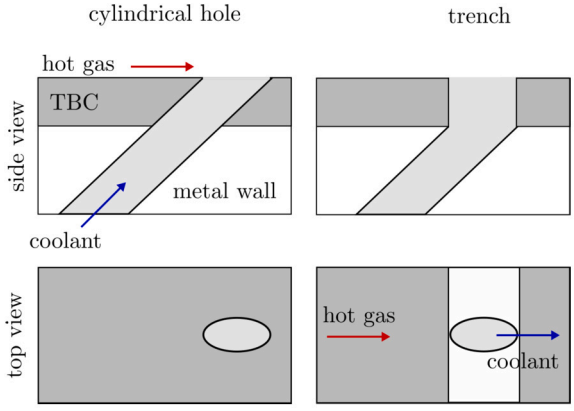

Fig. 1. Schematics of ordinary cylindrical and trenched film cooling designs.

lence intensity (Tu) at the combustor-turbine interface for rich burners typically ranges from 10% to 20% with an integral turbulence length scale (Λ) between 10-20 mm [12] where [13] reported large scale turbulence with $\Lambda/D = 3$, in which D is the diameter of the film cooling hole. The turbulence in rich burn combustors is isotropic due to the dilution jets [14], whereas in lean burn combustors, the swirling main flow is characterized by anisotropic turbulence [15].

Effusion cooling liners are used to reduce the temperature of gas turbine components, but their effectiveness can be compromised by the swirling main flow. Recent experimental and numerical studies have shown that cooling films created by cylindrical holes are periodically destroyed by the swirling main flow, leading to low film cooling effectiveness [16]. Carlson and Talmor [17] have found that increasing turbulence intensity from 3 to 22% in the hot gas above a film cooling slot can significantly reduce the cooling efficiency by almost 50%. Further investigations have shown that increased turbulence intensities also decrease film coolant coverage for both trenched and untrenched designs [18,19]. In another numerical study including LES and standard effusion cooling [20], turbulence intensities ranging from 0 to 20% were generated at the main hot gas inlet boundary using digital filters with a length scale ranging from 0 to $1D$. When turbulence was increased, it resulted in initial improvement of surface cooling in the vicinity of the hole, but there was a decrease in cooling effectiveness downstream of the hole. On the other hand, it was demonstrated by Schmidt and Bogard [13] that increased turbulence intensity enhances film cooling effectiveness for standard effusion designs. In addition, [21] showed that the heat transfer coefficient is influenced by both turbulence intensity and length scale. These analyses emphasize the importance of conducting experiments and CFD simulations with realistic inflow conditions.

In previous experimental investigations at our institute, active turbulence generators were incorporated into an existing film-cooling rig, which create turbulence intensities typical of gas turbine combustors [22,12]. The crucial parameters, such as turbulence intensity and turbulence length scale, were measured and calculated through hot-wire and numerical probes and deemed to be representative turbulence at the interface between the combustor and turbine. The active turbulence generators were employed in film cooling experiments conducted in this rig [23,24].

In our study the heat transfer coefficient ratio h_f/h_0 is of interest which is defined [25] through

$$h_f = \frac{\dot{q}}{(T_w - T_{aw})} \tag{2}$$

and the reference heat transfer coefficient (h_0) of a flat plate without film cooling [26]

$$h_0 = (\rho u_\infty c_p) \frac{0.03}{Re^{1/5} Pr^{2/3}} \left[1 - \left(\frac{x_d}{x + x_d}^{0.9}\right)\right]^{-1/9} \left(\frac{T_{aw}}{T_\infty}\right)^{-1/4} \tag{3}$$

In the equations $\dot{q}$ is the wall heat flux and T_w is the local wall temperature. Two experiments at identical inflow boundary conditions of hot gas and coolant with two different wall boundary conditions have to be run to determine the film cooling efficiency and the heat transfer coefficient [27]. Our CFD approach requires only one simulation to determine h_f which is elucidated in the numerical section. In a different numerical investigation, two simulations were performed to determine these parameters [28]. With respect to h_0 the distance from boundary

layer suction to film cooling injection is x_d. To accurately predict the heat transfer associated with film cooling, it is necessary to have information about both the adiabatic wall temperature and the heat transfer coefficient distribution [29].

The main purpose of film cooling is a reduction of the hot gas wall heat flux which is quantified by the Net Heat Flux Reduction ($NHFR$)

$$NHFR = 1 - \frac{h_f}{h_0} \cdot (1 - \eta\vartheta) \tag{4}$$

where

$$\vartheta = \frac{T_\infty - T_c}{T_\infty - T_w} \tag{5}$$

To achieve the reduction in hot gas wall heat flux, the desire is to increase $NHFR$ by decreasing the ratio of h_f to h_0 and decreasing the adiabatic wall temperature (T_{aw}) or equivalently, increasing the film cooling efficiency (η).

The goal of this research is to use LES to simulate trench-shaped film cooling designs at low turbulence boundary conditions in comparison with results using high turbulence boundary conditions created by the (numerical) turbulence grids [12]. The proposed novel trench design [6] has not been tested numerically at high turbulence boundary condition and no information regarding the net heat flux reduction is available. The focus is on the clarification of the accuracy of LES predictions of film cooling efficiency and heat transfer coefficients when applied to literature cases and on the investigation of effects of the turbulence level on these two quantities. To the knowledge of the authors, this is the first time that adiabatic film cooling efficiency, as well as the heat transfer coefficient and net heat flux reduction are determined by performing one LES simulation to investigate film cooling.

The paper is structured as follows: firstly, the numerical approach is described; secondly, the numerical approach is validated using previous experimental results; thirdly, results of the time-averaged and instantaneous LES solutions, including η, h_f/h_0, $NHFR$ at the wall and the flow field are presented, followed by the conclusion.

2. CFD approach

This subsection first presents the description of the numerical settings for the LES, the numerical domain, as well as boundary and initial conditions.

2.1. Solver, governing equations and numerical settings

In the following the implementation within the OpenFOAM v1912 solver *rhoPimpleFoam* is described based on [30]. LES resolves the large turbulence scales while the sub-grid scales necessitate modeling. Favre-averaging is applied to the original equations for compressible and other variable-density flows. Thus, the continuity equation (pressure-based implementation) and momentum equations result:

$$\frac{\partial \bar{\rho}}{\partial t} + \frac{\partial \bar{\rho}\tilde{u}_i}{\partial x_i} = 0 \tag{6}$$

$$\frac{\partial \bar{\rho}\tilde{u}_i}{\partial t} + \frac{\partial \bar{\rho}\tilde{u}_i\tilde{u}_j}{\partial x_j} = -\frac{\partial \bar{p}}{\partial x_i} + \frac{\partial}{\partial x_i}\left(\bar{\tau}_{ij} - \bar{\rho}(\widetilde{u_i u_j} - \tilde{u}_i\tilde{u}_j)\right) \tag{7}$$

By denoting $\tilde{u}_i$ as the filtered velocity component, and $\bar{\rho}$ and $\bar{p}$ as the averaged fluid density and pressure, respectively, the shear-stress tensor is estimated using the gradient diffusion hypothesis [31] (for Newtonian fluids) as:

$$\bar{\tau}_{ij} = 2\bar{\nu}\bar{\rho}\left(\widetilde{S}_{ij} - \frac{1}{3}\delta_{ij}\widetilde{S}_{kk}\right) \tag{8}$$

$$\widetilde{S}_{ij} = \frac{1}{2}\left(\frac{\partial \tilde{u}_i}{\partial x_j} + \frac{\partial \tilde{u}_j}{\partial x_i}\right) \tag{9}$$

where $\bar{\nu}$ represents the filtered kinetic viscosity, $\widetilde{S}_{ij}$ denotes the components of the rate-of-strain tensor, and δ_{ij} represents the Kronecker delta. The Boussinesq hypothesis [32] is employed to model the unresolved Reynolds stresses,

$$\widetilde{u_i u_j} - \tilde{u}_i\tilde{u}_j = \tau_{t,ij} = -2\nu_t\bar{\rho}\left(\widetilde{S}_{ij} - \frac{1}{3}\delta_{ij}\widetilde{S}_{kk}\right). \tag{10}$$

The sub-grid scale turbulence viscosity ν_t is simulated using the Wall-Adapting Local Eddy-viscosity (WALE) model [33], which is preferred due to its specific development for wall-bounded LES and successful application on film cooling flows [10,11,34,35].

The energy transport equation is expressed using the concept of sensible enthalpy $\widetilde{h}_s$. The equation can be stated as

$$\frac{\partial \bar{\rho}\tilde{h}_s}{\partial t} + \frac{\partial \bar{\rho}\tilde{u}_i\tilde{h}_s}{\partial x_i} + \frac{\partial \bar{\rho}\tilde{E}_k}{\partial t} + \frac{\partial \bar{\rho}\tilde{u}_i\tilde{E}_k}{\partial x_i} = \frac{\partial}{\partial x_i}\left(\bar{\alpha}\frac{\partial \widetilde{h}_s}{\partial x_i} + \alpha_t\frac{\partial \widetilde{h}_s}{\partial x_i}\right) + \frac{\partial \bar{p}}{\partial t} \tag{11}$$

where the left hand side contains the kinetic energy $\tilde{E}_k = 0.5|\tilde{u}_i|^2$. The right hand side contains the approximations for the filtered heat diffusion fluxes based on the thermal diffusivity $\bar{\alpha}$ and the modeled enthalpy fluxes on the sub-grid $\alpha_t = \nu_t/Pr_t$. The turbulent Prandtl number was set to $Pr_t = 0.85$ like in other LES studies [36,37]. Moreover, a preliminary study indicated similar results for $Pr_t = 0.7$, 0.85 and 1. From the sensible enthalpy the static temperature T and wall heat flux $\dot{q}_w$ were determined for isothermal walls. The equation of state for ideal gases was utilized to obtain the density field, JANAF polynomials to determine the specific heat c_p, while the two coefficient Sutherland model [38] was used to compute the mixture transport properties.

A transport equation for a passive scalar [39], was added to this solver.

$$\frac{\partial \bar{\rho}\widetilde{T}_a}{\partial t} + \frac{\partial \bar{\rho}\tilde{u}_i\widetilde{T}_a}{\partial x_i} = \frac{\partial}{\partial x_i}\left(\bar{\alpha}\frac{\partial \widetilde{T}_a}{\partial x_i} + \alpha_t\frac{\partial \widetilde{T}_a}{\partial x_i}\right) \tag{12}$$

The scalar represented the temperature field $\widetilde{T}_a$, which would be generated when using an adiabatic wall boundary condition. This allowed to determine the heat transfer coefficient and the film cooling efficiency using only one LES calculation. Further information is given when the boundary conditions are described in Section 2.3.

The presented equation system was solved for using the PIMPLE (PISO-SIMPLE) algorithm. The transport equation for a passive scalar was solved after the main PIMPLE iteration. After two iterations using the SIMPLE method, two pressure correction loops, and one non-orthogonal correction per time step, the initial residuals decreased to a value below $5 \cdot 10^{-6}$. To calculate the gradients on the cell faces, the Green-Gauss-based method and second-order linear interpolation (Gauss linear) were utilized. The second-order upwind scheme was used to discretize the advective terms of velocity, kinetic energy, static enthalpy and passive scalar, while the Gauss linear corrected scheme was used to describe the diffuse terms. Linear interpolation was applied from the cell center to the cell face. The explicit non-orthogonal corrected scheme was used to calculate the surface normal gradients. The second-order implicit scheme was used to discretize the time derivative terms. The maximum Courant number ranged from 0.6 to 0.9, resulting in a physical time-step size of approximately $1 \cdot 10^{-7}$ s. Five through flows were performed for initialization, and around 10 were performed to determine the time average which represented 1 period of the actively generated turbulence boundary condition which is elucidated in Section 2.3.

2.2. Computational domain, film cooling designs and mesh

The computational domain is depicted in Fig. 2. It represents the same dimensions of the experimental setup by Schreivogel et al. [6] and Straußwald et al. [18]. The dimensions are normalized by using the diameter (D) of the film cooling hole (which is 6 mm). The origin is located at the center of the domain on the film-cooled wall and at the downstream edge of the film cooling hole. The primary channel's inlet and outlet are situated $6D$ upstream and $29D$ downstream of the origin,

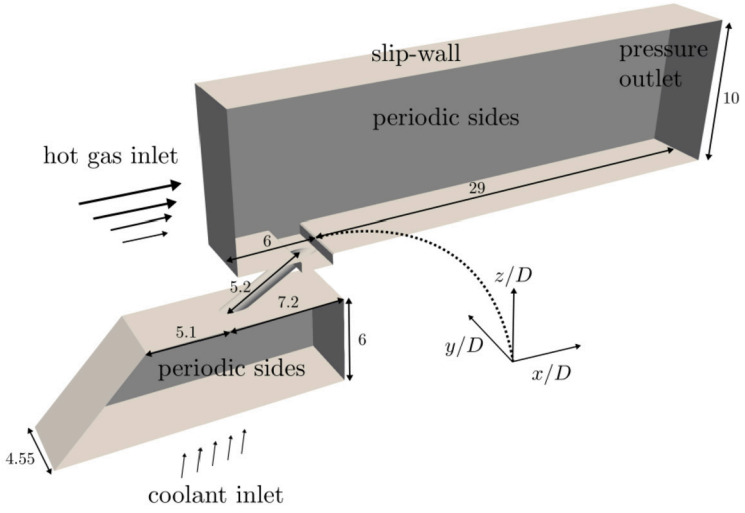

Fig. 2. Computational domain and boundary conditions. Dimensions are non-dimensionalized by the hole diameter (D).

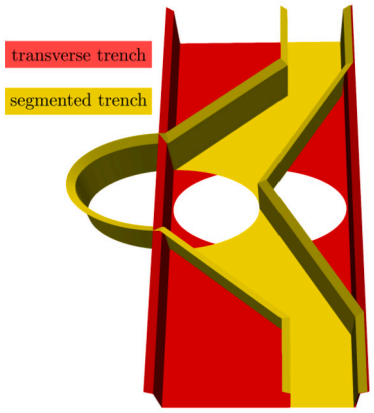

Fig. 3. Comparison of transverse and segmented trench designs. (For interpretation of the colors in the figure, the reader is referred to the web version of this article.)

respectively. The hole pitch value is $4.55D$. The film cooling hole has a length-to-diameter ratio of $5.16\overline{6}$, an inclined angle of 30°, and a sharp inlet edge, similar to experimental cases reported in [6] and [18].

Two film cooling designs with a cylindrical hole being embedded into trenches were investigated with a depth of $0.75D$. A third case without a trench, called standard effusion cooling, was investigated for reference. Fig. 3 shows the two trenched designs by Bunker et al. [4] and Schreivogel et al. [6]. The Bunker and Schreivogel design were both equipped with chamfers with an angle of 45° and an edge length of 0.7071 mm to increase the similarity with the experiments of Straußwald [18,23,24]. The transverse trench design by Bunker et al. is characterized by it's simple design which consists of a straight groove with the goal to increase the lateral spreading of the coolant, also reducing the tendency of jet lift-off particularly at higher momentum ratio. The purpose of the narrow and swept trench shape (called segmented trench) by Schreivogel et al. was to increase film cooling efficiency and lateral spreading of the coolant as well as to reduce hot gas ingestion into the trench. Especially, the hot gas entrainment into the trench is known for creating hot-spots in the trench and heating of the adjacent walls [40,41].

Symmetric meshes with respect to the symmetry-centerpane were created. The meshes were block-structured-based with hexahedral cells and were created for the trenches as well as for the untrenched standard cylindrical effusion cooling design. The number of cells varied between 7.2-14.4 millions ensuring the first cell within the viscous sublayer $y^+_{max} \leq 4.7$ with an average near wall resolution below $y^+_{avg} \leq 0.8$. Other studies successfully performed LES of film cooling flows with 6-12 million cells and a y^+ between 0.18-15 [10,35,42,43]. No adaptive mesh refining was applied.

In most of the numerical domain, the ratio (r_k) of resolved turbulent kinetic energy marked as k_{res}, in which

$$k_{res} = \frac{1}{2}(\overline{\tilde{u}'^2} + \overline{\tilde{v}'^2} + \overline{\tilde{w}'^2}) \tag{13}$$

to the overall turbulent kinetic energy (which encompasses time-averaged subgrid kinetic energy, $\overline{k_t}$ and time-averaged resolved velocity fluctuation, e.g. $\tilde{u}'$) exceeded 95%:

$$r_k = \frac{k_{res}}{k_{res} + \overline{k_t}} \tag{14}$$

satisfying the 80% lower limit value suggested by Pope [31] for a LES with near-wall resolution. In areas with a coarse mesh resolution (e.g. top of the domain, near the outlet), the proportion of turbulent kinetic energy is less than 80%. Details of the mesh topology and Pope criterion are given in Fig. 4.

2.3. Boundary and initial conditions

The boundary conditions closely resembled the ones of the experiments of Straußwald et al. [18] and are illustrated in Fig. 2. Possible backflow at the outlet was prevented by setting the velocity vector to zero for the relevant cells. The pressure at the outlet was set to 1 bar. The no-slip condition was applied on all walls except for the top of the main channel (slip condition). The lateral side patches were subjected to periodic boundary conditions. The values for the temperature and passive scalar at the test section inlet was set to $T_\infty = 373$ K and $T_c = 233$ K at the cooling plenum inlet, resulting in a gas turbine representative coolant to hot gas density ratio of $DR = 1.6$.

Different boundary conditions for the energy equation and transport equation of a passive scalar to determine (T_w) and (T_{aw}) were applied at the wall of the trench and the wall downstream of the trench. The energy equation (11) was solved including an isothermal boundary condition with $T_w = 223$ K which was 10 K below T_c. This leads to a value of $\vartheta = 0.93\overline{3}$ used to determine $NHFR$ (equation (4)). When solving for the transport equation of the passive scalar the zero gradient (adiabatic) boundary condition was applied. Gritsch et al. stated [27] that as long as the same inflow boundary conditions for the coolant and hot gas are applied the determination of h_f is valid for two different wall temperatures (e.g. T_w and T_{aw}) even at jet engine like density ratios.

The velocity at the coolant inlet was derived by the experimentally investigated momentum ratios of $I = 3.5$ and $I = 8.3$ where I is defined as

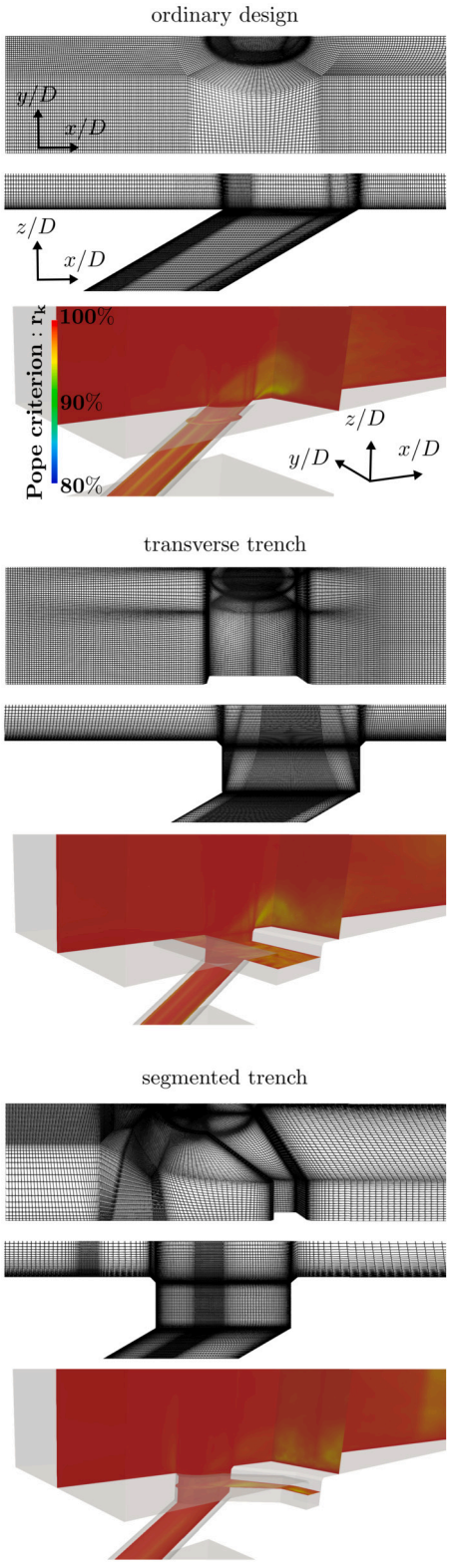

Fig. 4. Mesh details (top view of external wall and side view of centerplane) and Pope criterion (isometric view) of the three designs at $I = 3.5$ and high turbulence.

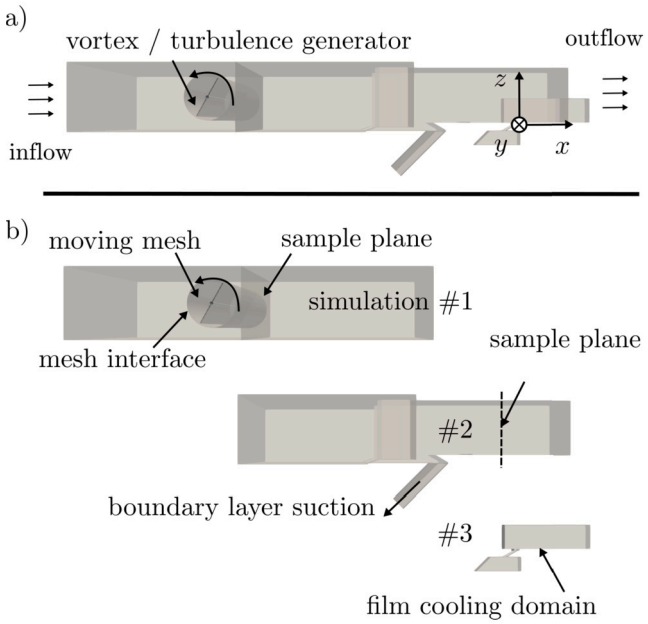

Fig. 5. Creation of the high turbulence boundary condition. Domains of the thermal wind tunnel including the vortex generator to create the turbulence boundary condition (a). Distribution of the LES simulations to three domains to reduce complexity (b).

$$I = \frac{\rho_c \overline{u}_c^2}{\rho_\infty \overline{u}_\infty^2} \tag{15}$$

The jetting effect [44] caused a maximum Mach number of 0.4 to be reached within the coolant hole. The maximum time step size due to the Courant number was limited at the sharp edge of the coolant inlet. Additionally, no turbulence intensity was applied at the coolant inlet. Turbulence is generated naturally within the coolant hole [45]. Two different boundary conditions (for low and high turbulence condition) were utilized at the main flow inlet. The first condition involved an average velocity profile at low turbulence conditions, which was determined from measurements conducted by Straußwald et al. [18]. This velocity profile can be characterized by a power-law profile with

$$u(z) = \overline{u}_\infty \cdot (z/\delta_{99})^{1/11} \quad , \; z \le \delta_{99} \tag{16}$$

where z is the wall normal distance and $\overline{u}_\infty$ is the main-stream velocity of 10.2 m/s. The thickness of the boundary layer was $\delta_{99} = 2D$. No turbulence intensity was applied at the inlet because of unknown turbulence length scale. The Reynolds number of the freestream flow, based on the diameter of the hole, was 2500.

The second and highly turbulent boundary condition was generated by LES simulations of a turbulence generator within the thermal wind tunnel shown in Fig. 5. Two precursor LES simulations (#1 and #2) of the thermal wind tunnel facility were performed as shown in Fig. 5b). The simulation #1 included a plate rotating at 160 rpm (called vortex generator (VG)) in a rectangular domain to create the turbulence field based on the approach shown in [12]. The rotation of the plate leads to a sinusoidal shape signal with additional higher frequencies. The velocity field was saved at a sampling plane within simulation #1. Next, this sampled boundary condition was applied in the numerical domain #2 representing the thermal wind tunnel including boundary layer suction. Upstream of the film cooling section the highly turbulent velocity field was saved to be reusable to perform simulations #3 of different film cooling designs. The results of the simulations #3 are investigated in this paper.

The time-averaged velocity $\overline{u}$, as well as turbulence intensity (Tu) and integral length scale (Λ) were determined from a simulation spanning a time duration of 4 plate rotations (8 signal periods) resulting in

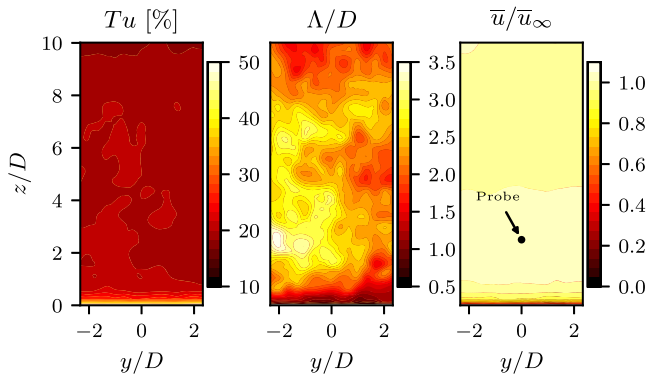

Fig. 6. Contours of the turbulence intensity, length scale and time-averaged main stream velocity at the inlet of the film cooling domain ($x/D = -6$). The location of the probe indicates the signal depicted in Fig. 8.

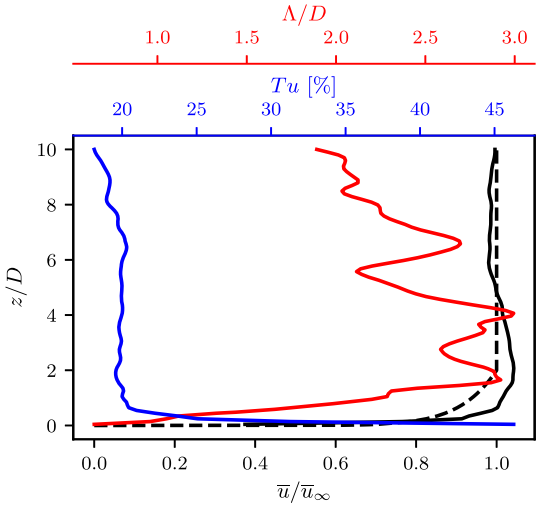

Fig. 7. Centerline boundary layer profiles of the high (-) and low turbulence (--) case.

Tu of around 20% and Λ between 0 to $3.5D$, respectively (Fig. 6) which matched engine like boundary conditions.

The turbulence quantities were derived after applying the triple decomposition instead of the Reynolds-decomposition onto the velocity signal to remove the low frequency component of the turbulence generator (which would have erroneously led to higher values of Tu and Λ as shown in [46]). The profiles of the centerline ($y/D = 0$) for both the low and high turbulence case are depicted in Fig. 7.

Fig. 8 depicts the unsteady time signal of a probe at the main flow inlet ($x/D = -6$, $y/D = 0$, $z/D = 2.5$, see Fig. 6) of the domain which is non-dimensionalized by the period length T_{VG} of the active vortex generator.

The periodicity is hard to detect in the near wall probes due to the effect of the boundary layer suction placed upstream of the coolant injection. However, probes placed farther away from the wall show periodicity and the distinct frequency of the turbulence generators in the time signal. Near and far placed probes show the turbulence generator rotation frequency.

After the initial transient phase of the LES in the film cooling domain (#3), the time average is taken over one period length of the vortex generator. The period length of $T_{VG} \approx 0.2$ s represents 10 main channel through flows. The experimental data showed little effect on the time averages if more than one period was used [47]. Moreover, during the simulation unsteady snapshots of the flow field where sampled to investigate unsteady behavior of the flow field and coolant distribution at

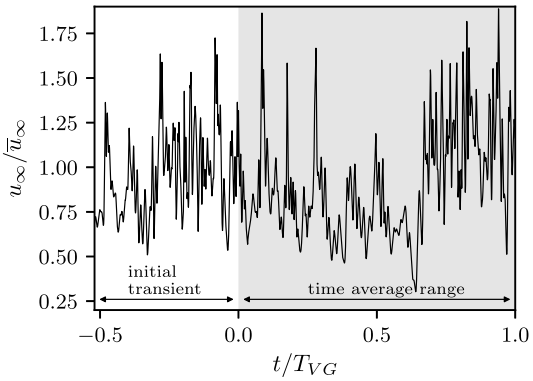

Fig. 8. Near wall velocity signal of probe created by the vortex generator at the domain inlet.

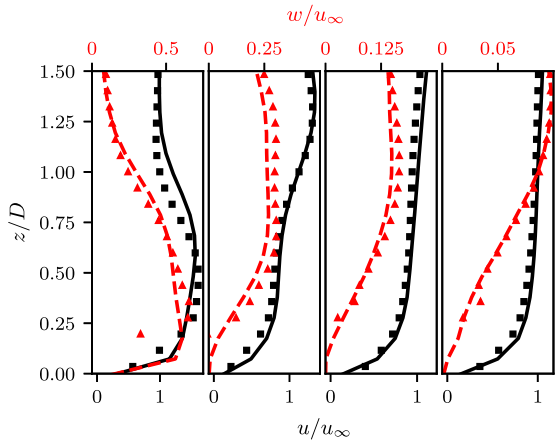

Fig. 9. Comparison of numerical (-, --) and experimental (■, ▲) [47] wall normal profiles of u/u_∞ and w/u_∞ at $x/D = [0, 2.5, 5, 7.5]$ using standard film cooling with no trench at $I = 3.5$ with actively generated turbulence boundary condition.

the wall. The simulations were initialized from RANS simulations with matching boundary conditions for each case.

3. Validation of numerical approach

In this section first the temperature and velocity profiles in the film cooling test section of LES simulations and TPIV measurements [47] are compared at actively generated high turbulence conditions. Subsequently, numerical results are compared to film cooling efficiency and heat transfer coefficient measurement results from the literature to determine the accuracy of the numerical approach.

With the actively generated turbulence boundary condition two profile series are shown at $I = 3.5$. No experimental data were available for the segmented trench at this boundary condition. First, results of the profiles of standard effusion cooling (no trench) are shown in Fig. 9. The numerical and experimental profiles of the wall normal velocity profiles are compared at $x/D = [0, 2.5, 5, 7.5]$. Excellent agreement of the boundary layer profile can be seen at all axial locations. Next, the trend of the normalized root mean square (RMS) of adiabatic temperature fluctuation $T_{a,RMS}$ and temperature θ which is defined as

$$\theta = \frac{T_\infty - T_a}{T_\infty - T_c} \tag{17}$$

are discussed in Fig. 10 for transverse trench. Good agreement is found as well, indicating that the LES is able accurately reproduce results from the experiment of Straußwald.

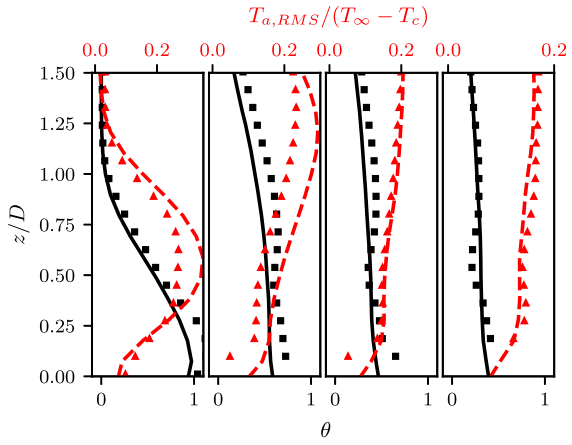

Fig. 10. Comparison of numerical (-, --) and experimental (■, ▲) [47] wall normal profiles of θ and $T_{RMS}/(T_\infty - T_c)$ at $x/D = [0, 2.5, 5, 7.5]$ using transverse trench at $I = 3.5$ with actively generated turbulence boundary condition.

No wall temperature and heat transfer coefficient measurements from Straußwald et al. were available. Thus, experimental data of the transverse and segmented trench at low turbulence boundary conditions from three earlier measurement campaigns were used: measurements at $DR = 2$ and 1.33 of Schreivogel et al. [6,48] and results of the transverse trench including the mentioned edge chamfer at $DR = 1.1$ of Lu et al. [49].

The flow boundary conditions are crucial when performing simulations and experiments and are summarized here briefly. For the simulations of the Schreivogel experiments a boundary layer velocity profile based on the power-law with an exponent of 1/6 and a boundary layer thickness of $\delta_{99} = 1.083D$ was applied at the hot gas inlet.

In the experiment of Lu et al. the boundary layer was described by a power law profile with an exponent of 1/7. However, no information regarding the turbulent boundary layer height was given. It was approximated to $\delta_{99} \approx 0.634D$ based on the development of the turbulent boundary layer [50] by the distance from boundary layer suction leading edge to the leading edge of the cooling film hole in the experiment. Both LES were performed with zero inlet turbulence level due low levels (1% and 2%, respectively) in the experiment and because of the lack of information regarding the turbulence length scale.

Fig. 11 shows the laterally averaged film cooling efficiency ($\overline{\eta}$) and heat transfer coefficient ratio ($\overline{h_f}/h_0$) downstream of the transverse trench of the performed LES simulations compared to Schreivogel and Lu's investigations [6,48,49].

The three numerical simulations show the same trend for $x/D < 2$ whereas at $I = 1$ the results do not depend on the density ratio. The experiments of Schreivogel and Lu at a momentum ratio of $I \approx 1$ with $DR = 2$ and $DR = 1.1$ show a similar trend of $\overline{\eta}$ for $x/D < 3$. Thus, the high discrepancy between the numerical and experimental results at $DR = 1.33$ are assumed in the accuracy of the experimental campaign as Schreivogel et al. [51] also showed that the jet trajectory of the film cooling jet emerging from the transverse trench does not depend on the density ratio. In general, the LES simulations overpredicted the film cooling efficiency measurements. This might be caused by differences in the shape of the trench edge (sharp, beveled or filleted and specific edge dimensions). Moreover, the trends of the film cooling efficiency are the exactly same for $I = 1$ and $I = 8$ (not shown) at $DR = 1.33$ for both experimental and numerical results.

Next, the results of heat transfer coefficient ratio are discussed for which no experimental results for the heat transfer coefficient ratio at $DR = 2$ are available. The CFD results of Lu's configuration match well with the experimental data for $x/D < 2$. Further downstream, the CFD underpredicts the heat transfer coefficient. Similar discrepancies of $\overline{\eta}$ and $\overline{h_f}/h_0$ were visible for $I = 3.7$ at $DR = 1.1$ and $I = 8$ at $DR = 1.33$ (not shown).

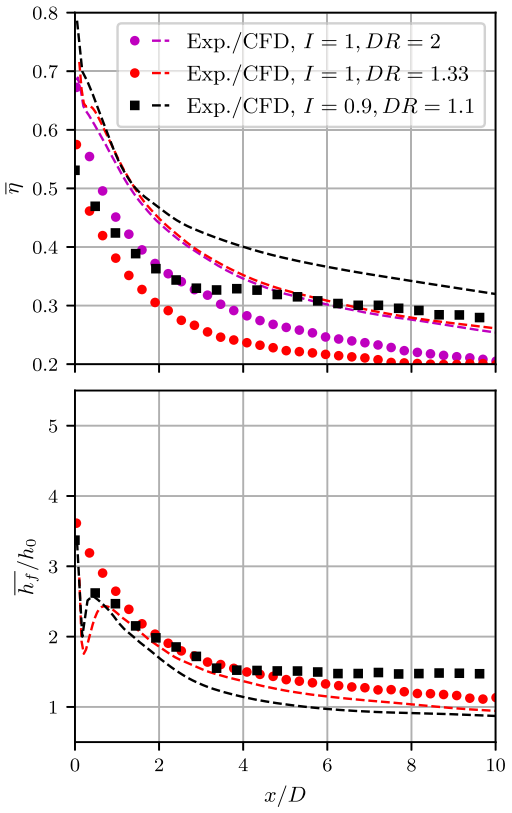

Fig. 11. Comparison of numerical and experimental [6,48,49] results of lateral averaged film cooling efficiency and heat transfer coefficient ratio using a transverse trench.

In the following the differences between simulation and experimental results of the segmented trench are discussed. The edges of segmented trench did not contain a chamfer in these LES simulations because pictures of the segmented trench indicated a relatively sharp edge. Fig. 12 shows the film cooling efficiency (η) and heat transfer coefficient ratio (h_f/h_0) of the performed LES simulations compared to Schreivogel investigations [6,48].

An excellent agreement between the LES and infrared thermography-based surface temperature measurements for both tested momentum ratios 1 and 8 at $DR = 2$ is visible. For $DR = 1.33$ one can see that the CFD overpredicts the film cooling efficiency like for the measurements of the transverse trench in the same measurement campaign [48]. The trend of the lateral film cooling distribution is similar. The differences between the experiments and CFD are not assumed to be an effect of the density ratio. Rather, a difference between experimental and numerical flow boundary conditions is assumed (boundary layer profile and turbulence properties) as well as uncertainties related to the trench edge shape (sharp or e.g. chamfered). Next, the results of heat transfer coefficient ratio are shown in Fig. 12 for $DR = 1.33$. No experimental results for the heat transfer coefficient ratio at $DR = 2$ are available. Both LES and experiment show the highest value of h_f/h_0 at $x/D \approx 1$ after which the heat transfer coefficient ratio is reducing.

The experimental uncertainties are given in each experimental campaign, whereas for the film cooling efficiency the maximum relative uncertainties were 8.7% ($DR = 2$), 7% ($DR = 1.33$) and the average uncertainty was 4.5% ($DR = 1.1$). The average uncertainty for the heat transfer coefficient measurements was 7% ($DR = 1.33$ and $DR = 1.1$). These uncertainties let us assume that large differences between the numerical and experimental results are due to systematical errors in the experiments of Schreivogel at $DR = 1.33$ and the unknown boundary layer profile for Lu's experiments at $DR = 1.1$. Additional and consistent experimental data with detailed descriptions of geometrical (edge

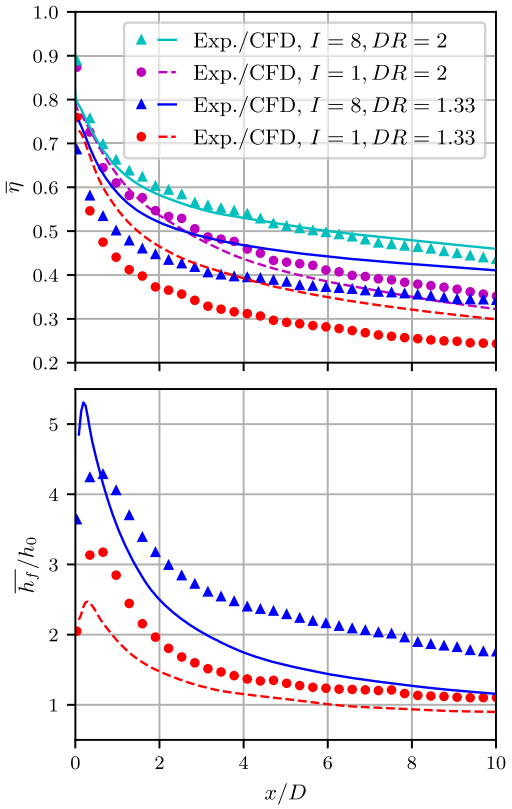

Fig. 12. Comparison of numerical and experimental [6,48] results of lateral averaged film cooling efficiency and heat transfer coefficient ratio using a segmented trench.

shape) and inflow boundary conditions (velocity profile, turbulence intensity and length scale) would be immensely important for the CFD community as accurate validation data. Ellis et al. [20] showed that by considering turbulence intensity and the turbulence length scale in the simulation agreement was improved with an experiment.

In conclusion, the numerical simulations of the transverse and segmented trench are able to predict matching (segmented trench at $DR = 2$) or similar trends of film cooling efficiency and heat transfer coefficient ratio at different momentum and density ratios.

4. Results of time averaged field

First, the results of the mean flow fields are analyzed to show the effects of the turbulence intensity and momentum ratio. Afterwards, the three film cooling designs are compared to each other.

4.1. Effect of momentum ratio and turbulence intensity

The influence of the turbulence intensity and momentum ratio on the lateral averaged film cooling efficiency, heat transfer coefficient ratio and net heat flux reduction over the axial distance (x/D) depending on the film cooling design is shown in Fig. 13.

The figure shows the trends for the standard effusion design indicated by a film cooling efficiency near $\eta = 0$ which is increasing for high main flow turbulence created by the vortex generator. Jet lift-off occurred for both tested momentum ratios and thus has a negligible influence on $\overline{\eta}$. The heat transfer coefficient ratio increases with increased turbulence intensity and momentum ratio whereas it is more affected by the increased turbulence intensity. With respect to $\overline{NHFR}$, increasing turbulence intensity or coolant mass flux and thus the momentum ratio leads to lower net heat flux reduction.

Fig. 13 shows the trends of the parameters of interests at the downstream wall for the transverse (middle column) and segmented (right column) trench design as well. At low turbulence conditions the effect of increased momentum ratio is low on the film cooling efficiency. At high turbulence boundary conditions the effect is more pronounced for the segmented trench which leads to a decrease in $\overline{\eta}$ by around 0.1 in the axial direction for the lower momentum ratio. The heat transfer coefficient ratio is mostly affected by the momentum ratio which is increasing for higher I. It shows little variation due to increased turbulence intensity. Downstream of $x/D > 3$ higher turbulence intensity leads to an increased heat transfer. The net heat flux reduction $\overline{NHFR}$ shows the same trend as with no trench.

The trends are similar for the tested momentum ratios and thus in the following the effect of turbulence is discussed for $I = 3.5$. In Fig. 14 the influence of turbulence on the normalized temperature θ is shown in the centerpane (xz-plane at $y/D = 0$) depending on the three designs standard effusion, transverse trench and segmented trench. The contour color and line (-) represent the high turbulence case whereas the results of the low turbulence simulations are shown by the dotted lines (- -).

For the hole without a trench (top) the jet lift-off is reduced due to increased turbulence and coolant is transported closer to the wall. Using a trench, the jet impacts on the trench wall directly. The coolant flow then can attach better to the downstream wall to provide a cooling film which is however reduced in efficiency by increased free-stream turbulence.

The contours of film cooling efficiency, heat transfer coefficient ratio and net heat flux reduction (top to bottom) at the wall are shown in Fig. 15. In general, higher turbulence levels result in increased diffusion of spanwise velocity, temperature and heat flux fluctuations [20]. In our study, for the ordinary hole case the film cooling efficiency is between 0 and 0.1 at increased turbulence. The lateral extent of η is reduced when no turbulence is present. Just downstream ($x/D < 1$) of the film cooling hole there is an area of slightly increased η due to the flow separation.

In comparison, the trenched cases show increased film cooling efficiency, especially in the lateral direction. The turbulence intensity reduces the axial extend of the film coolant and also diminishes the extent of the lateral spread. Thus, increased turbulence has the opposite effect for a trenched case compared to a standard effusion cooling at this momentum ratio.

In the case of standard effusion cooling, the heat transfer coefficient at high turbulence intensity is increased in the lateral direction compared to low turbulence intensity between $0 < x/D < 4$ and $y/D \pm 1.5$. Without turbulence in the main stream the lateral extent of increased heat transfer is only limited in the region between $y/D \pm 0.25$. For the trenched cases the turbulence intensity has only a negligible effect on the heat transfer as shown in the laterally averaged plots. The lateral spread of h_f/h_0 is very similar between these cases and is even increased without main stream turbulence for the segmented trench below $x/D < 1$ compared to the high turbulence intensity case as is also visible in Fig. 13.

Next, the resulting net heat flux reduction is discussed. For the ordinary hole case lateral regions of decreased $NHFR$ developed by increased turbulence intensity which correspond to the regions of increased heat transfer coefficient. In the case of the transverse trench an increased turbulence intensity lowers $NHFR$ at the sides between $y/D = 1$ to 2 and -1 to -2 downstream for $x/D < 2$. In these regions low adiabatic film cooling efficiency and relatively high heat transfer coefficient ratio are present. The segmented trench shows a lower $NHFR$ at the lateral location at $y/D \approx -1.5$ due to spatial asymmetry in the turbulence boundary condition (Fig. 6) in which higher intensity and length scales are present.

4.2. Effect of design

In this part the three film cooling designs are compared with each other. Fig. 16 depicts the three laterally averaged performance parameters of interest at high turbulence intensity. The segmented trench outperforms the other two designs which can also be seen in the 2D

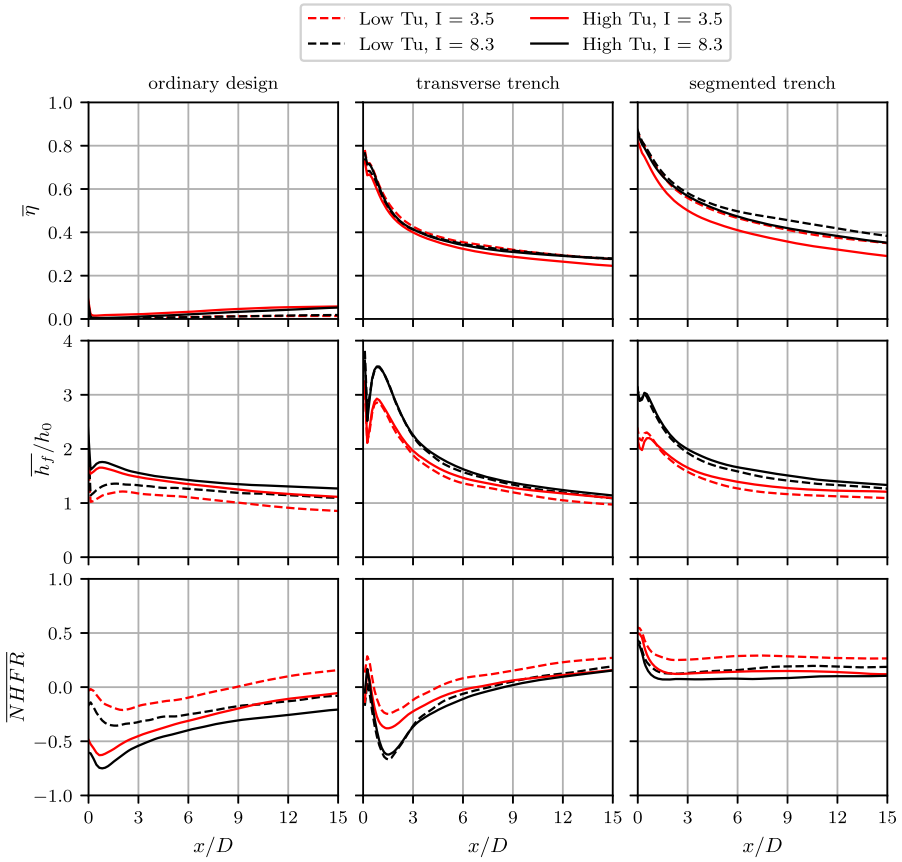

Fig. 13. Trend of the lateral averaged film cooling efficiency, heat transfer coefficient ratio and resulting net heat flux reduction depending on turbulence boundary condition and momentum ratio for standard effusion cooling (left column), transverse trench (center column) and segmented trench (right column).

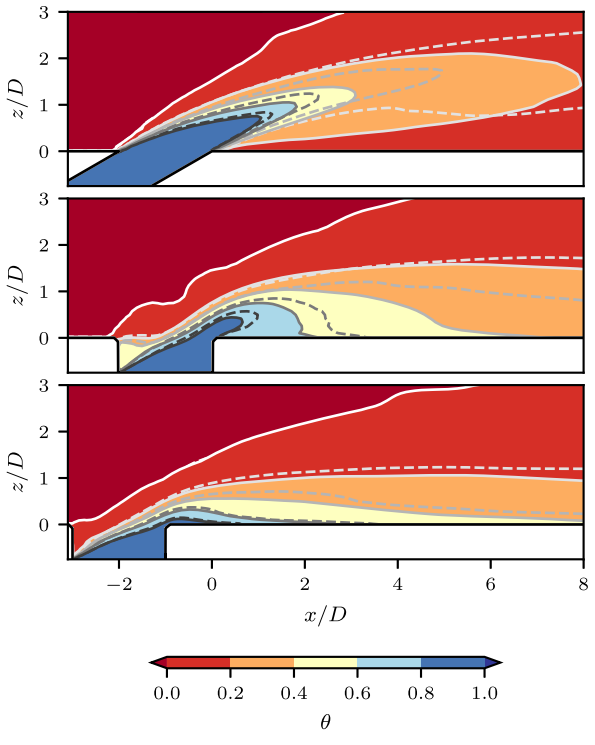

Fig. 14. Trend of the dimensionless temperature depending on low turbulence (- -), high turbulence (-) for standard effusion cooling (top), transverse trench (middle) and segmented trench (bottom). Momentum ratio $I = 3.5$.

wall distribution in Fig. 15. It has the highest film cooling efficiency, lower heat transfer coefficient than the transverse trench and thus the highest net heat flux reduction for both momentum ratios. The transverse trench has the highest heat transfer coefficient but due to high film cooling efficiency it outperforms the standard effusion design with respect to $\overline{NHFR}$. Moreover, only the segmented trench features a positive $\overline{NHFR}$ over the whole axial range whereas the transverse trench presents a positive $\overline{NHFR}$ only downstream of $x/D \approx 9$.

Fig. 17 depicts the lateral distribution of the three designs at the axial location $x/D = 3$ and 9. The segmented trench provides higher film cooling efficiency in the axial and lateral directions compared to the other designs. The heat transfer of the segmented design is lower than the transverse design at $x/D = 3$ and similar at $x/D = 9$. The net heat flux reduction is positive in the lateral direction for the segmented design except at $y/D \approx -1.5$ indicating homogeneous distribution of the time averaged cooling performance parameters due to the increased turbulence intensity and length scale at this location.

Next, axial cut contours at $x/D = 1, 3$ and 9 for each design at high turbulence intensity are shown in Fig. 18. The contours are colored in the normalized temperature θ and velocity vectors with the lateral and wall normal components (v, w) are added in black to indicate the rotation direction of vortices. In general, counter rotating kidney vortices are developing in the coolant hole [45] for each coolant design. At the plane just downstream of the ordinary film cooling design $(x/D = 1)$ the counter rotating kidney vortices emerging from the hole entrain hot gas from the main stream transporting it to the region near the wall. These vortices are propelling the coolant jet in a direction that moves it farther from the surface. The kidney vortices are weakening downstream but are still present at $(x/D = 9)$. Using the transverse trench these vortices are still visible at $x/D = 1$ and 3 but with a lower amplitude. Moreover, the coolant is very close to the wall but only in a

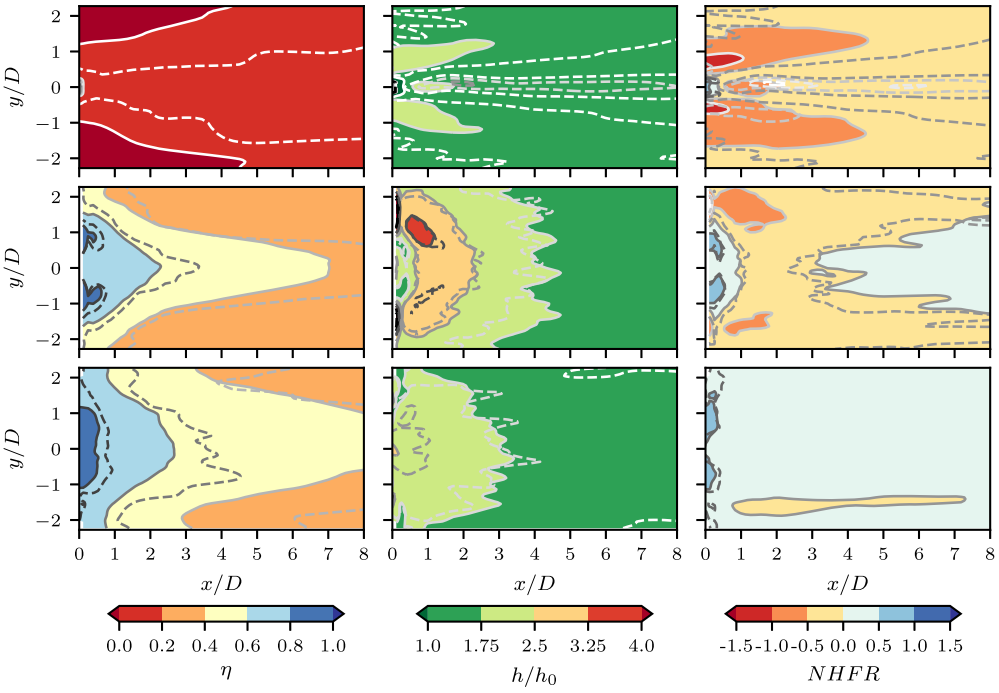

Fig. 15. Distributions of the film cooling efficiency, heat transfer ratio and resulting net heat flux reduction depending on low turbulence (- -), high turbulence (-) for standard effusion cooling (top), transverse trench (middle) and segmented trench (bottom). Momentum ratio $I = 3.5$.

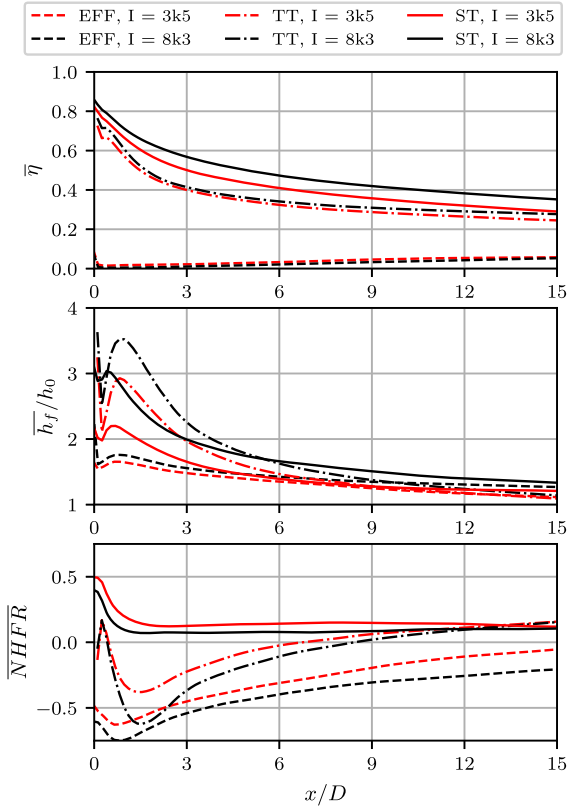

Fig. 16. Axial trend of the lateral averaged film cooling efficiency, heat transfer coefficient ratio and resulting net heat flux reduction depending on turbulence boundary condition and momentum ratio for standard effusion cooling (EFF), transverse trench (TT) and segmented trench (ST) at high turbulence intensity.

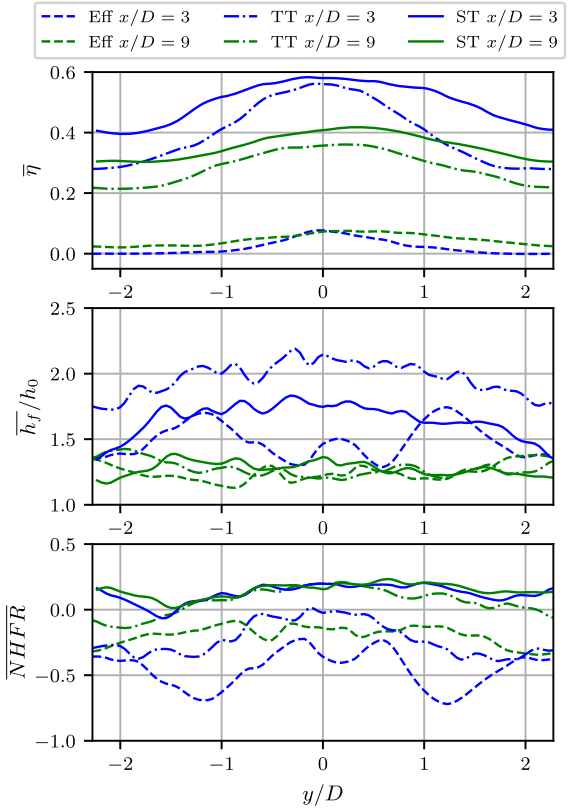

Fig. 17. Lateral distribution of the film cooling efficiency, heat transfer ratio and resulting net heat flux reduction at $x/D = 3$ and 9 depending on turbulence boundary condition and momentum ratio for standard effusion cooling (EFF), transverse trench (TT) and segmented trench (ST) at high turbulence intensity.

limited lateral range compared to the segmented trench. In the case of the segmented trench, the counter-rotating kidney vortices are barely visible in any of the planes. Both trenches form anti counter rotating vortices at the corners of the plane at $x/D = 1$ which were also noticed

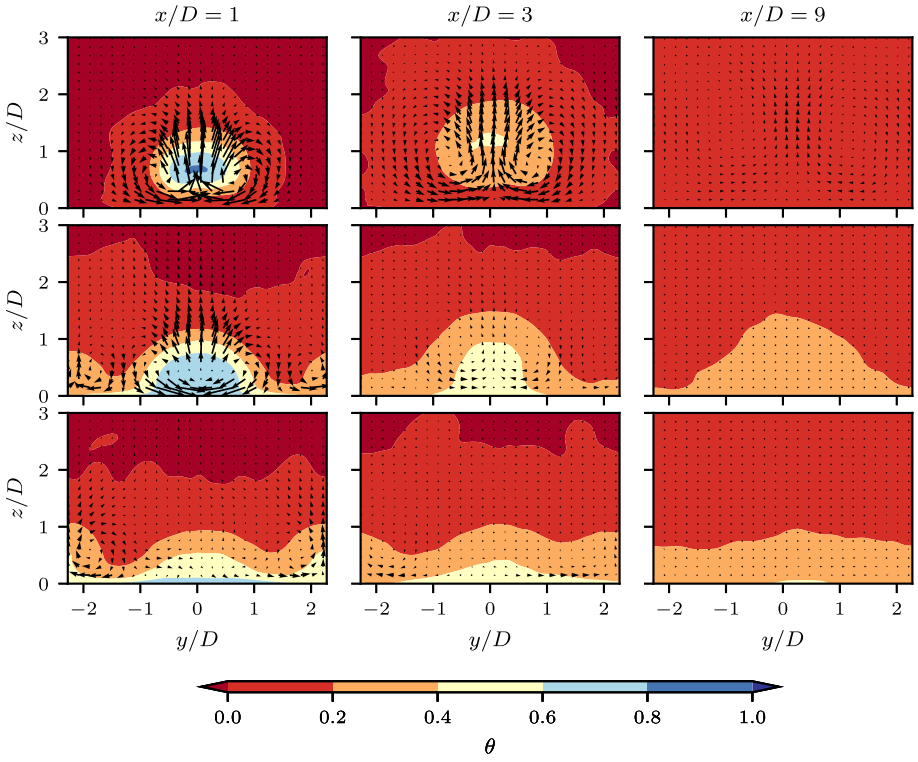

Fig. 18. Axials cuts of dimensionless temperature at $x/D = 1, 3, 9$ at high turbulence intensity for standard effusion cooling (top), transverse trench (middle) and segmented trench (bottom). Arrows result from the v and w velocity component. Momentum ratio $I = 3.5$.

in e.g. [10,52]. The presence of these side vortices results in increased amount of coolant being expelled from the trench (at $y/D \approx \pm 2$) onto the downstream wall. The wall normal extent of the coolant, described by θ, is higher for the transverse trench in the middle of the plane but is higher for the segmented trench at the corners.

To understand the effect of the axial, lateral and wall normal coolant distribution, the normalized temperature at high turbulence intensity is depicted in streamwise planes at multiple lateral position for the transverse and segmented trench in Fig. 19. In general, the coolant emerging from of the transverse trench achieves a higher trajectory (up to $z/D = 2$) providing a thicker coolant film in the lateral range ($-1 < y/D < 1$) compared to the segmented trench (up to $z/D = 1$). This is due to the shape of the transverse trench which offers a greater blockage area for the coolant exiting the hole whereas the wedge-shape of the segmented trench (compare the designs in Fig. 3) leads to a smaller coolant accumulation at the stagnation point and thus leads the most attached coolant at the downstream wall. Left and right of the trench's cooling hole ($y/D = -2.275$) more coolant is emerging from the segmented trench due to the anti counter rotating vortices. One could assume that the segmented trench is more affected by high turbulent boundary conditions compared to the transverse trench because the coolant film is thinner. However, the segmented trench in a time averaged sense leads to higher film cooling efficiency in the axial and lateral direction, reduces the transfer coefficient downstream of the trench and thus shows an overall positive $NHFR$ (Fig. 15). Furthermore, lower θ compared to the centerpane is visible in the transverse trench between $-2 \leq x/D \approx 0$ in the planes ($y/D = -1, -1.5, -2.275$). This effect is also present for the segmented trench but much less so due to the mentioned trench shape.

It can be explained by visualizing the wall normal velocity component w within the trench at the wall parallel plane $z/D \approx 0$ shown in Fig. 20. Areas with negative components indicate hot gas entrainment or ingestion into the trench which are present for both trench designs for 50 - 75% of the whole area. In general, hot gas ingestion may lead to lower film cooling efficiency within the trench (at the inner walls of the trench) which affects the adjacent walls through thermal conduction as well [40,41] and should be avoided. For both trenches, ingestion occurs above the coolant outlet since the perpendicular trench wall behaves like a backward facing step. Between $y/D = 1$ and 2 highest ingestion leads to lowest dimensionless temperature within the transverse trench which is visible in Fig. 19a), too. The ingestion is lower for the segmented trench.

5. Results of the instantaneous field

In the study conducted by Straußwald et al. [18], high turbulence conditions were employed, created by an active turbulence grid and the vortex generator also used for this study. All TPIV investigations were conducted at the centerpane ($y/D = 0$). Using the active turbulence grid and a resulting $I = 5.7$, results indicated that the time-averaged axial extent of the cooling film was shorter for the segmented trench in comparison to the transverse trench. Additionally, instantaneous images [47] revealed instances where the cooling film was significantly disturbed in the axial direction when the transverse trench was subjected to the vortex generator boundary condition. Based on these observations in the centerpane only, it was concluded that the segmented trench design was more susceptible to increased free stream turbulence compared to the transverse trench, and thus, the transverse trench would be a more suitable choice for cooling combustor liners. Straußwald et al. [18] mentioned as well that further investigations would be needed to clarify this statement.

To examine the impact of increased turbulence on film cooling efficiency in this numerical investigation, Fig. 21 displays time series of wall distributions of η for the transverse and segmented trench designs. The left and right columns present snapshots at the same time instances for the transverse and segmented trench, respectively. The time intervals between each snapshot range from 3.3 ms to 0.8 ms, corresponding to approximately 0.5TF to 0.1TF. The through flow time (TF) was defined over an axial range of 15D and was calculated as $TF = 15D/u_\infty$.

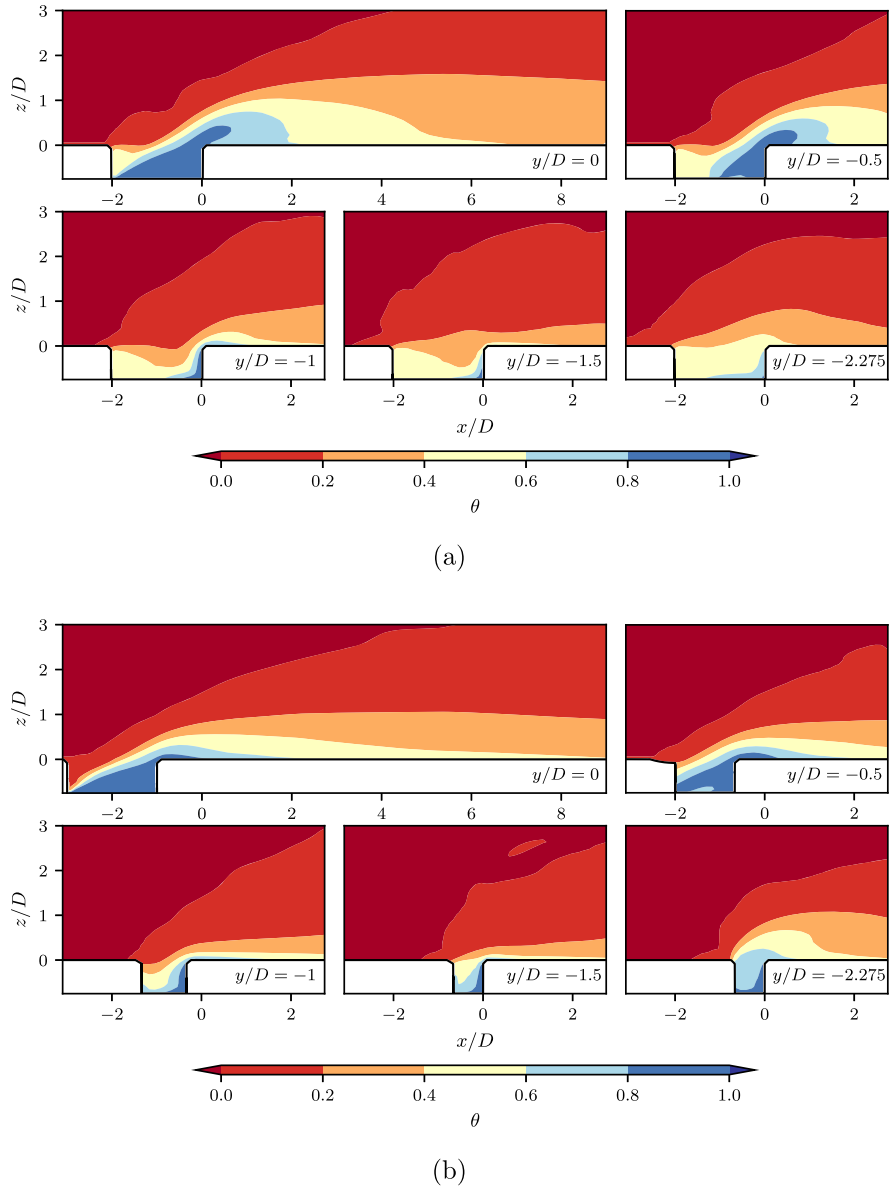

Fig. 19. Streamwise planes at different lateral positions of dimensionless temperature at high turbulence intensity for the transverse (a) and segmented (b) trench. Momentum ratio $I = 3.5$.

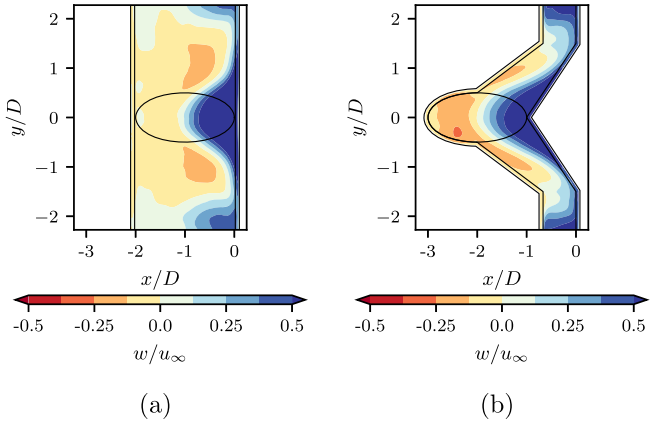

Fig. 20. Wall parallel cut at $z/D \approx 0$ to visualize hot gas ingestion (negative value of wall normal velocity w/u_∞) at $I = 3.5$ for the transverse trench (a) and segmented trench (b). Main flow with high turbulence.

The film cooling efficiency remained nearly unchanged in both the axial and lateral directions downstream of $x/D > 8$ across snapshots #1 to #5 for both the transverse and segmented trench designs. Therefore, the analysis primarily focuses on the coverage immediately downstream of the trenches.

In snapshot #1, the axial and lateral distribution of the coolant at the wall was best for both designs, leading to high values for η (Fig. 21). In the subsequent instant (#2), the axial extent of the film cooling efficiency was reduced for both designs. Furthermore, a hot spot emerged just downstream of the segmented trench (at $x/D = 0, y/D = 0$), resulting in a drop in η from above 0.9 within the range of 0.2 to 0.3. The transverse trench exhibited less sensitivity in the central region of the wall due to the higher trajectory of the coolant. However, it displayed significantly lower coolant coverage at the sides ($y/D \approx \pm 2$) compared to the segmented trench.

In instant #3, the hot spot downstream of the segmented trench shifted even further downstream ($x/D = 1-4, y/D = 0$). Moreover, brief hot spots emerged at both lateral sides where η experienced a drop within the range of 0.0 to 0.1. In comparison to snapshot #2, the trans-

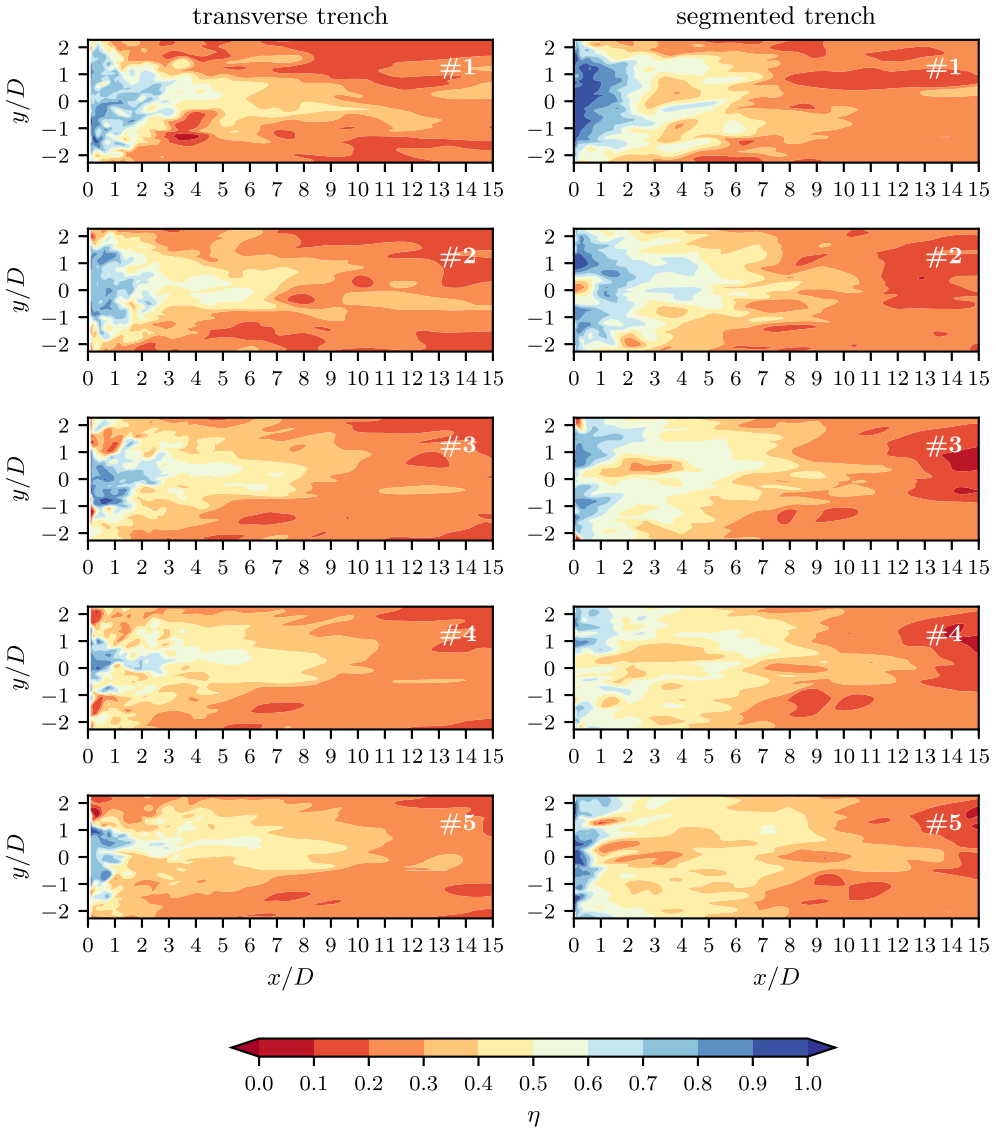

Fig. 21. Snapshots (#1 – #5) of the distributions of the film cooling efficiency at high turbulence for transverse trench (left column) and segmented trench (left column). Momentum ratio $I = 3.5$.

verse trench exhibited a further reduction in the lateral and axial extent of coverage at the sides.

In instant #4, the axial and lateral coverage of the transverse trench reached its minimum, with η ranging between 0.1 and 0.2. The hot spots located at the sides disappeared downstream of the segmented trench, but in the central region, the coverage was still low, resulting in $\eta >$ 0.3.

In the last instant of the time series (#5), the coolant coverage exhibited an increase immediately downstream of the trenches. However, in the downstream region of the transverse trench, a localized area was observed on one side between $x/D = 0.5$ and $y/D = 1 - 2$, indicating a deviation from uniform coverage.

Fig. 22 presents streamwise planes at lateral positions, including the centerpane, one outer plane ($y/D = -2.275$), and the intermediate position at $y/D = -1$, showcasing the normalized temperature distribution θ for both trench designs. These planes are utilized for further analysis and clarification.

At instant #1, the film cooling efficiency downstream of the trenches (for $x/D < 4$) was observed to be high. In all planes, it was evident that the coolant was being discharged from the trenches and adhering to the wall. Additionally, the wall-normal extent of the coolant in the centerpane ($y/D = 0$) was significant for both designs, with a greater extent observed for the transverse trench. The greater extent may lead to a potential reduction in sensitivity to main stream vortices in this region due to a higher momentum of the coolant jet.

Snapshots #2 – 4 revealed a decrease in film cooling efficiency at the sides for the transverse trench design (Fig. 21). In snapshot #3 of (Fig. 22), the lateral xz-planes of θ illustrated a reduced wall-normal extent of the coolant. Additionally, at positions ($y/D = -1$ & -2.275), a lower amount of coolant or coolant with lower θ was observed exiting the transverse trench. Conversely, for the segmented trench design in snapshot #3, the inadequate film cooling efficiency at the sides could be attributed to observations in the $y/D = -2.275$ plane. Here, despite the presence of coolant, hot gas temporarily reached the wall beneath the coolant film. Simultaneously, the main flow exhibited a notably high negative wall-normal velocity component in the centerpane (not shown). Consequently, less coolant was discharged from the segmented trench, resulting in an almost non-existent coolant film between $y/D =$ 0.5 to -1 (in Snapshot #4). Nonetheless, a very thin layer of coolant was still observed near the wall. This suggests that Straußwald et al.'s experimental investigations faced challenges when drawing conclusions about film cooling efficiency using results from the xz-centerpane.

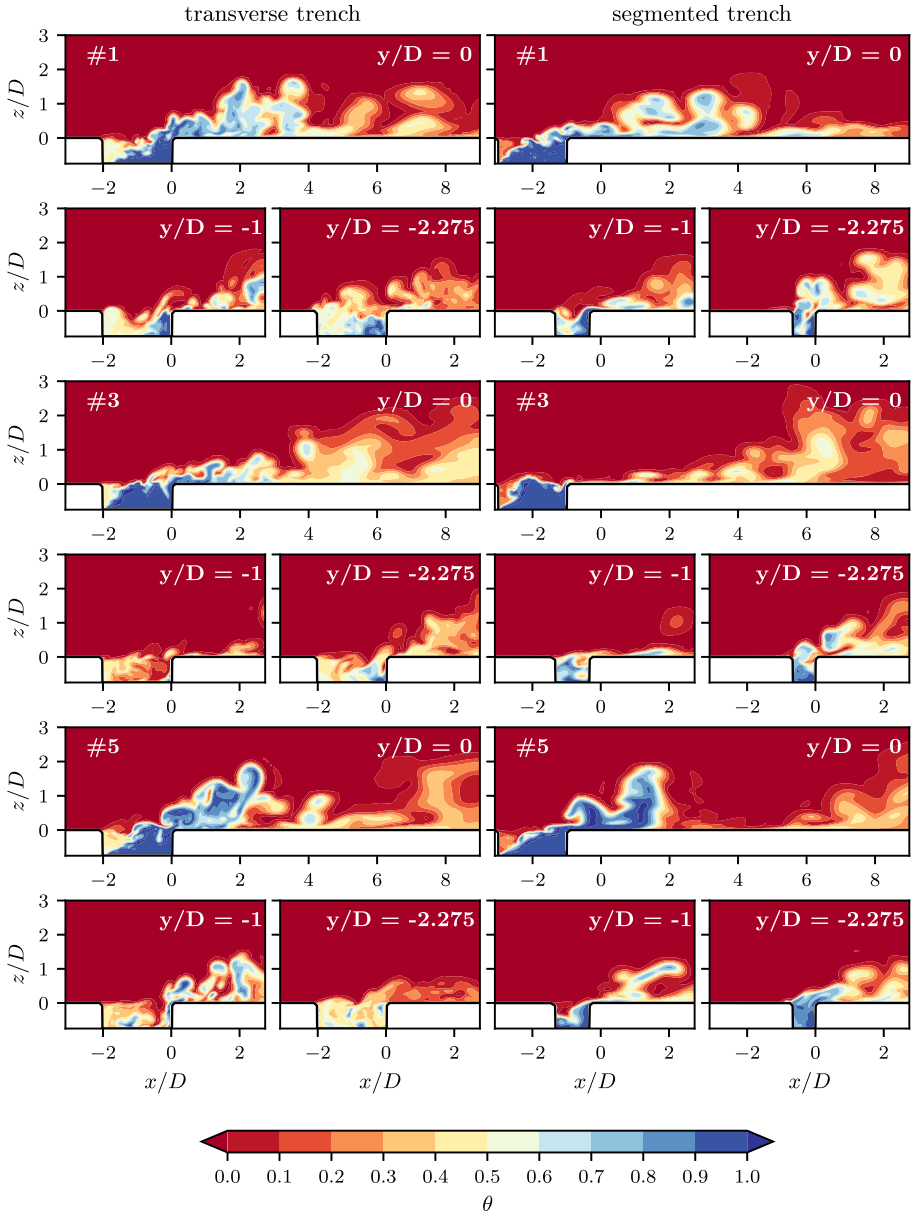

Fig. 22. Snapshots (#1, #3, #5) at three lateral planes of the distributions of the normalized temperature at high turbulence for transverse trench (left column) and segmented trench (right column). Momentum ratio $I = 3.5$.

In snapshot #5, the negative wall normal component of the main stream velocity has disappeared, resulting in an extremely lifted jet trajectory for both trench designs. For the segmented trench, coolant remains attached just downstream of the trench along the lateral direction. However, it is worth noting that the near wall temperature gradient is very high in the case of the segmented trench. As a result, the coolant between $1 < x/D < 2$ in the centerpane has not yet reached the wall, leading to a low film cooling efficiency in that region. The hot spot observed at the side of the transverse trench can be attributed to a strong mixing of coolant and hot gas within the trench, along with a lower amount of coolant exiting the trench at that particular instant.

6. Conclusion

LES simulations were employed to examine three film cooling configurations, including designs with and without a trench, under varying levels of main stream turbulence. By solving the energy equation and the transport equation of a passive scalar, the study was able to determine important parameters such as adiabatic film cooling efficiency, heat transfer coefficient, and net heat flux reduction which are rarely available from experimental investigations.

The numerical approach was validated by three experiments from the literature. The best agreement with the measurements was seen for the simulations of the segmented trench. The film cooling efficiency downstream of the transverse trench was overpredicted which is assumed due to the sensitivity of the trench's downstream located edge shape. The results of the experiment of Schreivogel et al. [48] at $DR = 1.33$ do not agree with the trend of the other two literature cases making it difficult to validate the CFD with respect to the heat transfer coefficient. The LES simulations were able to predict the laterally averaged trend and absolute values of the heat transfer coefficient just downstream of the trench for Lu's experiment. Additional and consistent experimental validation data (η and h_f/h_0) would hold immense significance for the CFD community.

The time-averaged results suggested that higher levels of turbulence intensity lead to a decrease in the effective length of the cooling film

across both trench designs, reducing η, whereas the ordinary design exhibited higher η due to increased mixing caused by lift-off of the jet. For all designs h_f was increasing and $NHFR$ was reducing with increased main stream turbulence. The heat transfer coefficient increased with both turbulence intensity and momentum ratio, with turbulence intensity having a greater effect for ordinary cooling designs and momentum ratio for trenched designs.

Increasing turbulence intensity or momentum ratio led to a lower net heat flux reduction for all designs. The lateral extent of the coolant was decreased for the trenched designs when turbulence intensity was increased leading to lower $NHFR$ at these lateral locations. With respect to the trench designs, increased turbulence intensity increased the heat transfer in the axial direction but reduced it just downstream of the trenches. Comparing the three designs, only the segmented trench design exhibited positive net heat flux reduction regardless of turbulence intensity and momentum ratio, outperforming the other designs. This is in contrast to experimental results of Straußwald et al. [18,24] in the centerpane in which the transverse trench outperformed the segmented trench. This discrepancy between the experimental observations and LES results may be attributed to limitations in measurement accuracy near the wall. The results obtained from LES demonstrated that, despite the absence of apparent cooling coverage in the xz-centerpane, coolant can still effectively cover the wall.

In the axial planes downstream of the cooling hole the counter rotation vortices were present at the center for the ordinary and transverse trench. The design of the segmented trench made the counter rotating vortices disappear. Both trench designs exhibited hot gas ingestion which should be avoided by changing the design. More hot gas entrainment occurred for the transverse design due to larger trench area. The segmented trench produced a thinner cooling film and more intense lateral cooling spread. At the sides of this trench more coolant was ejected compared to other lateral locations due to the stagnation point adjacent between holes which effect was enhanced due to the wedge-shape. The coolant exiting the middle of the transverse trench featured a larger wall-normal spread which made it less susceptible to main stream turbulence compared to the thinner cooling film of the segmented trench.

The instantaneous results further investigated this susceptibility to main stream turbulence. Hot spots were visible at certain instances in time. The segmented trench exhibited hot spots located in the middle of the wall. For the transverse trench hot spots only appeared at the sides downstream of the trench due to more coolant leaving the trench at this location providing a thicker coolant film. Similar unsteady results were shown in Straußwald et al.'s experiments [18,24].

Future studies could encompass the examination of momentum ratios relevant to turbines, the impact of potential manufacturing tolerances (such as the edge shape of trenches) and the comparison of novel trench designs [37] or alternative cooling designs with fan-shaped cooling holes.

CRediT authorship contribution statement

Lukas Fischer: Roles/Writing – original draft, Writing – review & editing, Data curation, Software, Investigation, Methodology, Project administration.

Michael Pfitzner: Funding acquisition, Writing – review & editing, Methodology, Project administration, Supervision.

Declaration of competing interest

The authors declare the following financial interests/personal relationships which may be considered as potential competing interests:
Lukas Fischer reports financial support was provided by Deutsche Forschungsgemeinschaft (DFG project number PF 443/7-1). Lukas Fischer reports equipment, drugs, or supplies was provided by Gauss Centre for Supercomputing e.V. under grant pn73ji. Lukas Fischer, Michael Pfitzner reports article publishing charges was provided by Universität der Bundeswehr München.

Data availability

Data will be made available on request.

Acknowledgement

Axel Buck for his support on the digitization of Schreivogel's and Lu's experimental 2D data to determine correctly lateral averaged plots. The authors gratefully acknowledge the Gauss Centre for Supercomputing e.V. (www.gauss-centre.eu) for funding this project by providing computing time on the GCS Supercomputer SUPERMUC-NG at Leibniz Supercomputing Centre (www.lrz.de) under grant pn73ji. The work was sponsored by the Deutsche Forschungsgemeinschaft (DFG project number PF 443/7-1). Moreover, we acknowledge financial support by Universität der Bundeswehr München.

References

[1] R.S. Bunker, A review of shaped hole turbine film-cooling technology, J. Heat Transf. 127 (4) (2005) 441–453, https://doi.org/10.1115/1.1860562.
[2] D.G. Bogard, K.A. Thole, Gas turbine film cooling, J. Propuls. Power 22 (2006) 249–270, https://doi.org/10.2514/1.18034.
[3] T. Wang, S. Chintalapati, R.S. Bunker, C.P. Lee, Jet mixing in a slot, Exp. Therm. Fluid Sci. 22 (1) (2000) 1–17, https://doi.org/10.1016/S0894-1777(00)00010-8.
[4] R.S. Bunker, Film cooling effectiveness due to discrete holes within a transverse surface slot, in: Volume 3: Turbo Expo 2002, Parts A and B, ASMEDC, Amsterdam, the Netherlands, 2002, pp. 129–138.
[5] H.I. Oguntade, G.E. Andrews, A. Burns, D. Ingham, M. Pourkashanian, CFD predictions of single row film cooling with inclined holes: influence of hole outlet geometry, in: Proceedings of ASME Turbo Expo 2010: Power for Land, Sea and Air, Glasgow, UK, 2010, p. 15.
[6] P. Schreivogel, B. Kröss, M. Pfitzner, Study of an optimized trench film cooling configuration using scale adaptive simulation and infrared thermography, in: Proceedings of ASME Turbo Expo 2014, American Society of Mechanical Engineers, Düsseldorf, Germany, 2014, V05BT13A003.
[7] Y. Huang, J.-z. Zhang, C.-h. Wang, Shape-optimization of round-to-slot holes for improving film cooling effectiveness on a flat surface, Heat Mass Transf. 54 (6) (2018) 1741–1754, https://doi.org/10.1007/s00231-017-2272-4.
[8] S. Sperling, L. Christensen, R. Celestina, R. Mathison, H. Aksoy, J. Liu, J. Nickol, Coupling of Mainstream Velocity Fluctuations with Plenum Fed Film Cooling Jets, vol. 84973, American Society of Mechanical Engineers Digital Collection, 2021, V05AT12A024, Virtual, Online.
[9] P. Kalghatgi, S. Acharya, Modal analysis of inclined film cooling jet flow, J. Turbomach. 136 (8) (2014) 081007, https://doi.org/10.1115/1.4026374.
[10] R. Hou, F. Wen, Y. Luo, X. Tang, S. Wang, Large eddy simulation of film cooling flow from round and trenched holes, Int. J. Heat Mass Transf. 144 (2019) 13, https://doi.org/10.1016/j.ijheatmasstransfer.2019.118631.
[11] A. Zamiri, S.J. You, J.T. Chung, Large eddy simulation of unsteady turbulent flow structures and film-cooling effectiveness in a laidback fan-shaped hole, Aerosp. Sci. Technol. 100 (2020) 16, https://doi.org/10.1016/j.ast.2020.105793.
[12] L. Fischer, M. Straußwald, M. Pfitzner, Analysis of large eddy simulations and 1D hot-wire data to determine actively generated main flow turbulence in a film cooling test rig, J. Turbomach. 144 (11) (2022) 111003, https://doi.org/10.1115/1.4054778.
[13] D.L. Schmidt, D.G. Bogard, Volume 4: Heat Transfer; Electric Power; Industrial and Cogeneration, American Society of Mechanical Engineers, Birmingham, UK, 1996, p. 7.
[14] M. Folk, R.J. Miller, J.D. Coull, The impact of combustor turbulence on turbine loss mechanisms, J. Turbomach. 142 (9) (2020) 091009, https://doi.org/10.1115/1.4047615.
[15] C. Hassa, L. Voigt, M. Schroll, J. Heinze, C. Willert, I. Bagchi, Friedrichshafen, Deutsche Gesellschaft für Luft- und Raumfahrt - Lilienthal-Oberth e.V., 2018, p. 10.
[16] T. Lenzi, L. Palanti, A. Picchi, T. Bacci, L. Mazzei, A. Andreini, B. Facchini, Time-resolved flow field analysis of effusion cooling system with representative swirling main flow, J. Turbomach. 142 (6) (2020) 061008, https://doi.org/10.1115/1.4046181.
[17] L. Carlson, E. Talmor, Gaseous film cooling at various degrees of hot-gas acceleration and turbulence levels, Int. J. Heat Mass Transf. 11 (11) (1968) 1695–1713, https://doi.org/10.1016/0017-9310(68)90048-3.
[18] M. Straußwald, T. Sander, C. Abram, M. Pfitzner, Investigating the influence of mainstream turbulence and large vortices on gas turbine trenched film cooling flows using planar temperature-velocity imaging, J. Turbomach. 144 (10) (2022) 101013, https://doi.org/10.1115/1.4054215.

[19] P.H. Wilkins, S.P. Lynch, K.A. Thole, T. Vincent, S. Quach, E. Kaufman, Experimental investigation into the effect of a ceramic matrix composite surface on film cooling, in: Volume 6A: Heat Transfer — Combustors; Film Cooling, American Society of Mechanical Engineers Digital Collection, Rotterdam, Netherlands, 2022.
[20] C.D. Ellis, H. Xia, Impact of inflow turbulence on large-eddy simulation of film cooling flows, Int. J. Heat Mass Transf. 195 (2022) 14, https://doi.org/10.1016/j.ijheatmasstransfer.2022.123172.
[21] K. Dullenkopf, R.E. Mayle, An Account of Free-Stream-Turbulence Length Scale on Laminar Heat Transfer, American Society of Mechanical Engineers, The Hague, Netherlands, 1994, V004T09A026.
[22] A. Bakhtiari, T. Sander, M. Straußwald, M. Pfitzner, Active Turbulence Generation for Film Cooling Investigations, American Society of Mechanical Engineers, Oslo, Norway, 2018, V05CT19A026.
[23] M. Straußwald, T. Sander, A. Bakhtiari, M. Pfitzner, High-Speed Velocity Measurements of Film Cooling Applications at High-Turbulence Main Flow Conditions, American Society of Mechanical Engineers, Oslo, Norway, 2018, V05CT19A027.
[24] M. Straußwald, C. Abram, T. Sander, F. Beyrau, M. Pfitzner, Time-resolved temperature and velocity field measurements in gas turbine film cooling flows with mainstream turbulence, Exp. Fluids 62 (1) (2020) 17, https://doi.org/10.1007/s00348-020-03087-2.
[25] R.J. Goldstein, Film Cooling, Advances in Heat Transfer, ISSN 0065-2717, vol. 7, Elsevier, 1971, pp. 321–379.
[26] S. Baldauf, A. Schulz, S. Wittig, High-resolution measurements of local heat transfer coefficients from discrete hole film cooling, J. Turbomach. 123 (4) (2001) 749–757, https://doi.org/10.1115/1.1387245.
[27] M. Gritsch, S. Baldauf, M. Martiny, A. Schulz, S. Wittig, The superposition approach to local heat transfer coefficients in high density ratio film cooling flows, in: Volume 3: Heat Transfer; Electric Power; Industrial and Cogeneration, American Society of Mechanical Engineers Digital Collection, Indianapolis, Indiana, USA, 1999, V003T01A048.
[28] N. Rosafio, S. Salvadori, D.A. Misul, M. Baratta, M. Carnevale, C. Saumweber, Effect of Self-Sustained Pulsation of Coolant Flow on Adiabatic Effectiveness and Net Heat Flux Reduction on a Flat Plate, American Society of Mechanical Engineers Digital Collection, 2021.
[29] B. Sen, D.L. Schmidt, D.G. Bogard, Film cooling with compound angle holes: heat transfer, J. Turbomach. 118 (4) (1996) 800–806, https://doi.org/10.1115/1.2840937.
[30] H.G. Weller, G. Tabor, H. Jasak, C. Fureby, A tensorial approach to computational continuum mechanics using object-oriented techniques, Comput. Phys. 12 (6) (1998) 620–631, https://doi.org/10.1063/1.168744.
[31] S.B. Pope, Turbulent Flows, 7th edition, Cambridge University Press, Cambridge, UK, 2010.
[32] D.C. Wilcox, Turbulence Modeling for CFD, 2nd edition, DCW Industries, La Cañada, California, 1998.
[33] F. Ducros, N. Franck, T. Poinsot, Wall-adapting local eddy-viscosity models for simulations in complex geometries, in: Numerical Methods for Fluid Dynamics VI, Jan. 1998.
[34] R. Hou, F. Wen, S. Wang, Y. Luo, X. Tang, Large eddy simulation of the trenched film cooling hole with different compound angles and coolant inflow orientation effects, Appl. Therm. Eng. 163 (2019) 114397, https://doi.org/10.1016/j.applthermaleng.2019.114397.
[35] L. Yang, F. Satta, D. Barsi, P. Zunino, Y. Luan, Numerical Investigation of Laidback Fan-Shaped Film Cooling Holes with Large Eddy Simulation, American Society of Mechanical Engineers, Rotterdam, Netherlands, 2022, V06AT12A045.
[36] P. Johnson, J. Kapat, Large eddy simulations of a cylindrical film cooling hole, in: 50th AIAA Aerospace Sciences Meeting Including the New Horizons Forum and Aerospace Exposition, American Institute of Aeronautics and Astronautics, Nashville, Tennessee, 2012.
[37] L. Fischer, D. James, S. Jeyaseelan, M. Pfitzner, Optimizing the trench shaped film cooling design, Int. J. Heat Mass Transf. 214 (2023) 124399, https://doi.org/10.1016/j.ijheatmasstransfer.2023.124399.
[38] W. Sutherland, The viscosity of gases and molecular force, Lond. Edinb. Dublin Philos. Mag. J. Sci. 36 (223) (1893) 507–531, https://doi.org/10.1080/14786449308620508.
[39] P. Sagaut, Large Eddy Simulation for Incompressible Flows - An Introductions, 3rd edition, Scientific Computation, Springer-Verlag, Berlin/Heidelberg, 2006.
[40] F.T. Davidson, D.A. Kistenmacher, D.G. Bogard, Film cooling with a thermal barrier coating: round holes, craters and trenches, in: Proceedings of ASME Turbo Expo 2012, ASME, Copenhagen, Denmark, 2012, pp. 1757–1768.
[41] L. Fischer, A. Sanchez, F. Schleich, F. Feller, R. Raffelt, M. Pfitzner, Conjugate Heat Transfer of Cylindrical and Trenched Film Cooling Designs with Array Jet Impingement, American Society of Mechanical Engineers Digital Collection, Rotterdam, Netherlands, 2022, V06AT12A011.
[42] G. Bidan, D. Nikitopoulos, Film-cooling jets analyzed with proper orthogonal decomposition and dynamic mode decomposition, in: 43rd Fluid Dynamics Conference, Fluid Dynamics and Co-Located Conferences, American Institute of Aeronautics and Astronautics, San Diego, CA, 2013.
[43] S. Agarwal, L. Gicquel, F. Duchaine, N. Odier, J. Dombard, D. Bonneau, M. Slusarz, Large Eddy Simulation Based Optimization of a Fan-Shaped Cooling Hole Geometry to Enhance Cooling Performance, American Society of Mechanical Engineers, Rotterdam, Netherlands, 2022, V06AT12A007.
[44] J.H. Leylek, R.D. Zerkle, Discrete-jet film cooling: a comparison of computational results with experiments, J. Turbomach. 116 (3) (1994) 358–368, https://doi.org/10.1115/1.2929422.
[45] S. Acharya, D. Houston Leedom, Large eddy simulations of discrete hole film cooling with plenum inflow orientation effects, J. Heat Transf. 135 (1) (2013) 011010, https://doi.org/10.1115/1.4007667.
[46] L. Fischer, M. Straußwald, M. Pfitzner, Analysis of LES and 1D Hot-Wire Data to Determine Actively Generated Main Flow Turbulence in a Film Cooling Test Rig, American Society of Mechanical Engineers Digital Collection, 2021.
[47] M. Straußwald, Experimentelle Untersuchung von Filmkühlung unter brennkammertypischen Strömungsbedingungen, Ph.D. thesis, Universität der Bundeswehr München, Neubiberg, 2021.
[48] P. Schreivogel, M. Pfitzner, Heat transfer measurements downstream of trenched film cooling holes using a novel optical two-layer measurement technique, J. Turbomach. 138 (3) (2016) 031003, https://doi.org/10.1115/1.4031919.
[49] Y. Lu, A. Dhungel, S.V. Ekkad, R.S. Bunker, Effect of trench width and depth on film cooling from cylindrical holes embedded in trenches, J. Turbomach. 131 (2009) 1–13, https://doi.org/10.1115/1.2950057.
[50] F.M. White, Fluid Mechanics, 4th edition, McGraw-Hill, 1998.
[51] P. Schreivogel, B. Kröss, M. Pfitzner, Density ratio effects on the flow field emanating from cylindrical effusion and trenched film cooling holes, in: Proceedings of ASME Turbo Expo 2014, Volume 5B: Heat Transfer, American Society of Mechanical Engineers, Düsseldorf, Germany, 2014, V05BT13A002.
[52] Y. Lu, S.V. Ekkad, Understanding the effect of trenching on film cooling, in: ASME/JSME 2007 Thermal Engineering Heat Transfer Summer Conference, vol. 3, ASMEDC, Vancouver, British Columbia, Canada, 2007, pp. 591–596.